AGU ADVANCING EARTH AND SPACE SCIENCE

Space Weather

RESEARCH ARTICLE
10.1029/2020SW002560

Observations and Modeling Studies of Solar Eclipse Effects on Oblique High Frequency Radio Propagation

M. L. Moses[1,2], L. J. Kordella[1,3], G. D. Earle[1], D. Drob[3], J. D. Huba[4], J. M. Ruohoniemi[1], S. G. Shepherd[5], and V. Sivakumar[1]

[1]Bradley Department of Electrical and Computer Engineering, Virginia Polytechnic Institute and State University, Blacksburg, VA, USA, [2]Department of Physics and Astronomy, Dartmouth College, Hanover, NH, USA, [3]Naval Research Laboratory, Washington, DC, USA, [4]Syntek Technologies, Fairfax, VA, USA, [5]Thayer School of Engineering, Dartmouth College, Hanover, NH, USA

Key Points:
- The eclipsed ionosphere has a significant effect on the horizontal and vertical propagation of obliquely incident HF radio waves
- HF propagation through the eclipsed ionosphere is modeled using ray tracing in conjunction with empirical ionospheric models
- Eclipsed ionosphere models with different wind fields suggest that meridional winds redistribute plasma more effectively than zonal winds

Correspondence to:
M. L. Moses,
magdalina.l.moses.gr@dartmouth.edu

Citation:
Moses, M. L., Kordella, L. J., Earle, G. D., Drob, D., Huba, J. D., Ruohoniemi, J. M., et al. (2020). Observations and modeling studies of solar eclipse effects on oblique high frequency radio propagation. *Space Weather*, *18*, e2020SW002560. https://doi.org/10.1029/2020SW002560

Received 9 JUN 2020
Accepted 21 SEP 2020
Accepted article online 25 SEP 2020

Abstract The total solar eclipse over the continental United States on 21 August 2017 offered a unique opportunity to study the dependence of the ionospheric density and morphology on incident solar radiation at different local times. The Super Dual Auroral Radar Network (SuperDARN) radars in Christmas Valley, Oregon, and Fort Hays, Kansas, are located slightly southward of the line of totality; they both made measurements of the eclipsed ionosphere. The received power of backscattered signal decreases during the eclipse, and the slant ranges from the westward looking radar beams initially increase and then decrease after totality. The time scales over which these changes occur at each site differ significantly from one another. For Christmas Valley the propagation changes are fairly symmetric in time, with the largest slant ranges and smallest power return occurring coincident with the closest approach of totality to the radar. The Fort Hays signature is less symmetric. In order to investigate the underlying processes governing the ionospheric eclipse response, we use a ray-tracing code to simulate SuperDARN data in conjunction with different eclipsed ionosphere models. In particular, we quantify the effect of the neutral wind velocity on the simulated data by testing the effect of adding/removing various neutral wind vector components. The results indicate that variations in meridional winds have a greater impact on the modeled ionospheric eclipse response than do variations in zonal winds. The geomagnetic field geometry and the line-of-sight angle from each site to the Sun appear to be important factors that influence the ionospheric eclipse response.

1. Introduction

The plasma density in the ionosphere is dependent on the intensity of incident sunlight, which creates plasma by ionizing neutral atmospheric particles. At night the ionosphere experiences a decrease in plasma density at all altitudes because production of ions is greatly attenuated, while recombination rates of electrons and ions remain high. When the Sun is obscured during an eclipse, a similar decrease in the density of the ionosphere is observed, especially at low altitudes where the recombination process is fast. However, the effect differs from the normal nightly decrease in plasma density since it is limited by the short time interval over which the eclipse blocks most of the sunlight and the fact that the corona remains visible throughout an eclipse. The onset of an eclipse is also more gradual than sunrise/sunset effects at low latitudes and midlatitudes, and eclipse paths have an apparent eastward motion that contrasts sharply with the steady westward motion associated with the terminators. All of these factors suggest that during an eclipse the ionosphere will not respond spatially or temporally as it does during sunrise/sunset conditions and will not experience decreases in electron density that are as significant as those that occur overnight.

Since the dawn of radio wave probes in the early 1900s, remote sensing experiments have been carried out to observe the unique ionospheric phenomena that occur during eclipses. On 21 August 2017 a total solar eclipse occurred over a narrow path that stretched from Oregon to South Carolina; it was observable as a partial eclipse over the entire continental United States, as shown in Figure 1. Since it passed over a region of the Earth that has a large concentration of ionospheric sounding instruments, it provided unique opportunities to observe interesting ionospheric effects at a high temporal cadence.

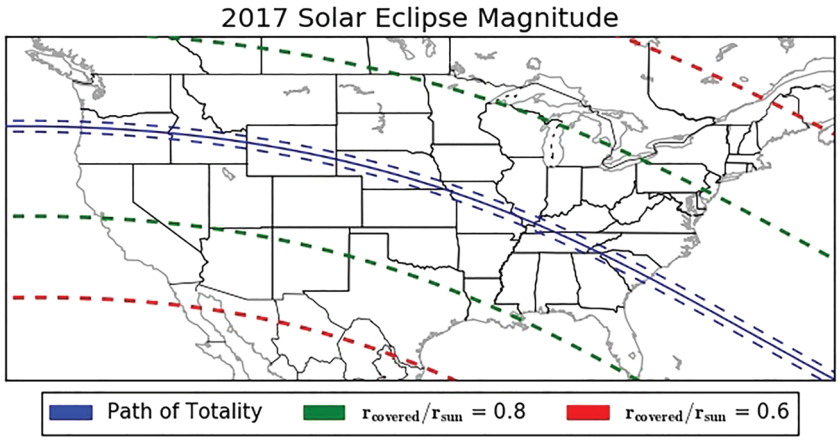

Figure 1. The 2017 eclipse path of totality (solid blue line) and contour lines showing boundaries for 60% (red dashed lines) and 80% (green dashed lines) fractional obscuration maxima (data from Xavier M. Jubier at https://xjubier.free.fr/en/site_pages/SolarEclipsesGoogleEarth.html).

Experiments during eclipses have previously shown that their ionospheric effects can vary as functions of magnetic latitude, time of day, solar zenith angle, and geomagnetic conditions (Bowhill, 1970; Hulburt, 1939; Rishbeth, 1969; Stankov et al., 2017). Results from such studies indicate that there are significant large-scale spatial effects on the ionosphere that extend well outside the umbra region. For example, the Special Sensor Ultraviolet Spectrographic Imager (SSUSI) instrument aboard the TIMED satellite observed a depleted airglow region roughly 1,000 km in diameter around the eclipse path of totality during the 29 March 2006 solar eclipse over western Africa (Y. Zhang, personal communication, June 16, 2015). Even when ionospheric measurements are made under similar conditions, the results sometimes appear contradictory (e.g., Afraimovich et al., 2002; Bowhill, 1970). Despite some inconsistencies, commonly observed effects of eclipses include decreases in the ionospheric plasma density in both the *E* and *F* regions, rapid disappearance of the *D* region in totally eclipsed regions, and changes in the height of the peak plasma density of the ionospheric *F* layer (Afraimovich et al., 2002; Evans, 1965a, 1965b).

For example, the Chilton ionosonde in Great Britain observed a significant decrease in foF2 (proportional to the square root of the electron density) during the 11 August 1999 solar eclipse eclipse, with reductions in *F* region plasma density of roughly 40% relative to the value given by the International Reference Ionosphere (IRI) model for that date (Afraimovich et al., 1965b, 2002). Other studies have indicated that ionospheric eclipse responses at a given magnetic latitude also vary with solar zenith angle (Chen et al., 2013; Chuo, 2013; Pitout et al., 2013; Sivakumar, 2018; Stankov et al., 2017). Since the motion of plasma along magnetic flux tubes into the depleted, eclipsed regions of the ionosphere is an important factor in the ionospheric eclipse response, the alignment of the Sun relative to the magnetic field during the eclipse will affect how much plasma is readily available to refill the depleted regions. More recently, there is evidence from the 2017 eclipse that a G condition may occur in the ionosphere coincident with the eclipse, with significant consequences for high-frequency (HF) oblique propagation (Bullett & Mabie, 2018).

In this paper we use data from select midlatitude Super Dual Auroral Radar Network (SuperDARN) radars coupled with ray tracing and geophysical modeling to help understand the physics of the ionosphere during the 2017 North American eclipse. We first describe the experiment and the radars and then interpret the radar signatures using a ray-tracing code coupled with a first-principles flux tube-coupled model of ionospheric responses to variations in sunlight during the eclipse.

2. Experiment Description and Analysis Approach

2.1. SuperDARN Overview

SuperDARN is a network of high-latitude and midlatitude coherent HF radars that measure ionospheric irregularities and structures. Each dual-radar SuperDARN site comprises independently operating westward looking and eastward looking radars. Each radar employs a phased-array antenna system that is electrically steerable, allowing the radar to form a beam at a given azimuth that is narrow in the horizontal direction

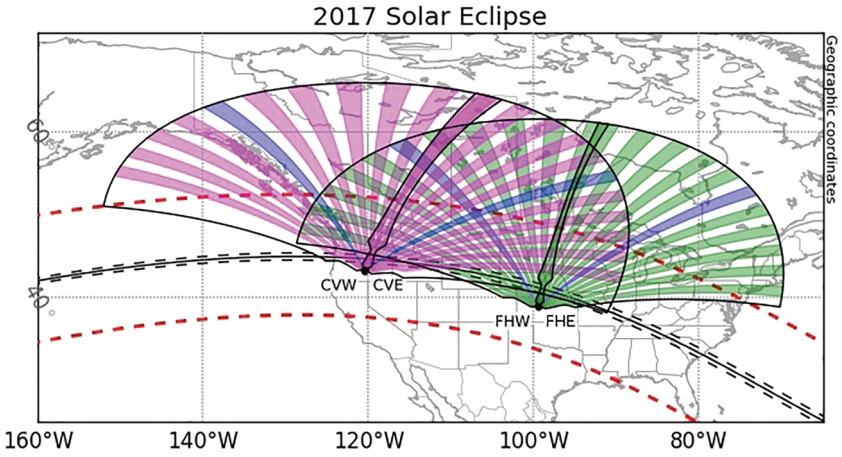

Figure 2. SuperDARN radar beams at Christmas Valley (magenta) and Fort Hays (green) intersect the 2017 eclipse path (black) and the boundary line of 80% eclipse obscuration (red). The camping beams for the eastward and westward halves of each radar are highlighted in blue (see text).

and broad in the vertical direction. A set of discrete beams forms the fan-shaped field of view (FOV) at each site. SuperDARN operates by sending out successive pulses along discrete azimuths and measuring the scattered signal that returns to the radar. Several quantities can be determined from the measurements including signal-to-noise ratio (SNR), Doppler line-of-sight velocity, spectral width of the signal, and angle of arrival (i.e., elevation angle) (not available from Fort Hays radars) (Nishitani et al., 2019).

SuperDARN primarily measures two types of scatter, ground scatter and ionospheric scatter. Ionospheric scatter occurs when the outgoing ray is coherently reflected back to the radar from a plasma structure in the ionosphere. In contrast, ground scatter signals are refracted through the ionosphere to the ground, where they are reflected back to the radar along a similar ionospheric refracted path. Signals with low Doppler velocities and small spectral widths are typically flagged as ground scatter (Nishitani et al., 2019). SuperDARN radars bin the measured scatter by time of arrival, corresponding to bins of ranges from the radar called range gates. The size of these range bins (ΔR) is typically about 45 km, with the first range gate located about 180 km from the radar (Nishitani et al., 2019). All SuperDARN data products are publicly available and can be accessed and analyzed using tools in the Data and Visualization Toolkit-Python (DaViTPy) software package (Ribeiro et al., 2020).

2.2. Eclipse Operations

The dual-radar SuperDARN sites in Christmas Valley, Oregon (CV), and Fort Hays, Kansas (FH), have FOVs that intersect the path of totality of the 2017 eclipse, as shown in Figure 2. On the date of the eclipse these four radars, Christmas Valley West (CVW), Christmas Valley East (CVE), Fort Hays West (FHW), and Fort Hays East (FHE), operated at a transmit/receive frequency of about 10.5 MHz in every other beam mode. In this mode, a radar makes measurements on every other beam azimuth (highlighted magenta and green in Figure 2), returning to the camping beams (highlighted in blue in Figure 2) between successive azimuth changes. This operating mode is designed to maximize the temporal resolution for each camping beam while continuing to make lower-resolution observations over nearly 180° in azimuth.

Figure 2 illustrates the spatial coverage of each beam with eclipse data. The radars started operating in this mode around 12:00 UT on 21 August and continued operating until around 0:00 UT on 22 August. It should be noted that the ground track of the umbra of the eclipse (black line in the figure) lies very close to the transmitter antennas at both radar sites. The solar zenith angle moves this umbra region slightly northward at ionospheric altitudes, but the majority of the radar propagation path through the ionosphere takes place in the partially eclipsed penumbra region lying northward of the ground track. The only exceptions to this were the most eastward directed beams from CVE and the westward beams from FHW.

2.3. Propagation Modeling

Propagation of radio waves can be modeled by ray tracing, in which the radio wave is treated as a discrete ray propagating through the ionosphere. At each time step in the simulation the dispersion relation in the

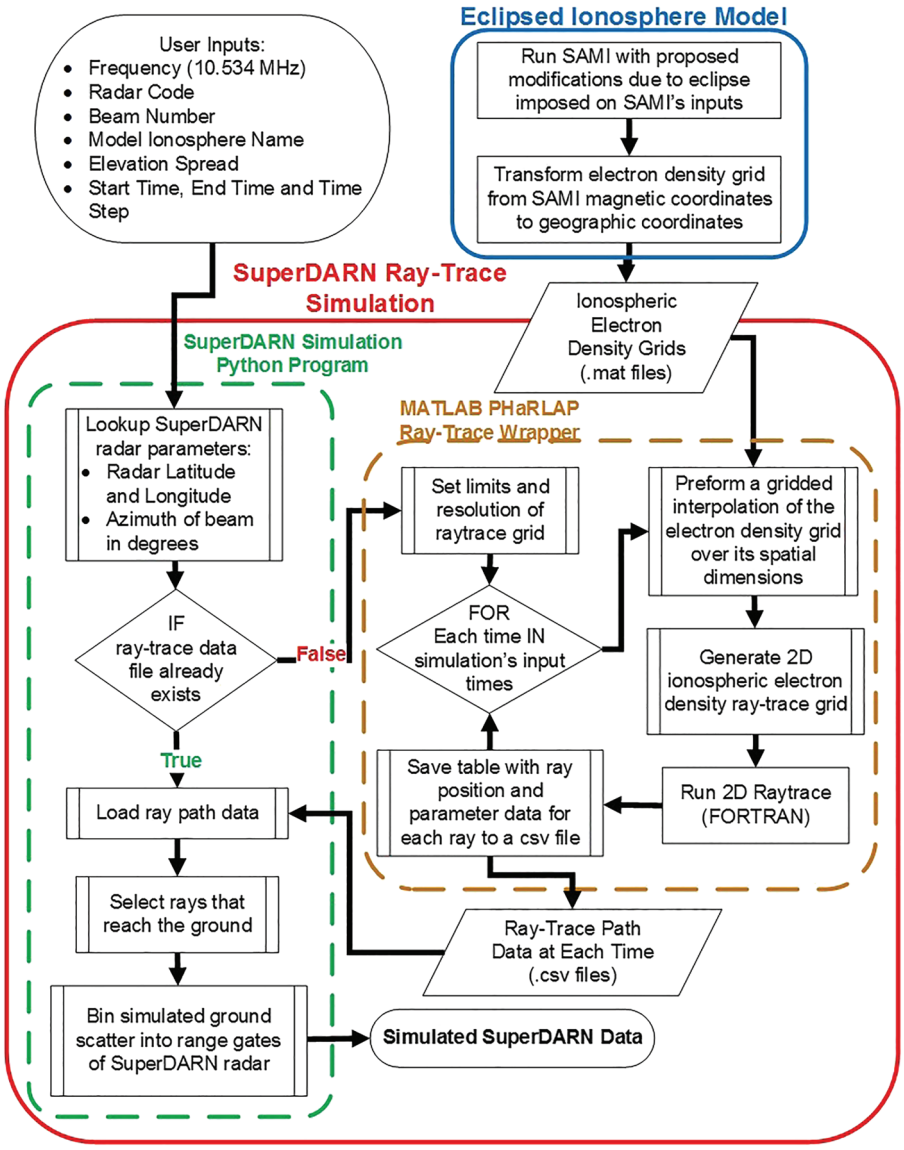

Figure 3. Flowchart of the simulation algorithm.

ionospheric model is solved to find a new wavevector direction for the beam, and this process is iterated to model the refraction of the ray along the ionospheric path. Simulated SuperDARN data can therefore be extracted from the output of a ray trace model that is initialized with the radar operating parameters (i.e., operating frequency, elevation spread, beam azimuth, latitude, longitude, etc.). In this study we use the HF propagation toolbox known as PHaRLAP (Provision of High-frequency Raytracing Laboratory for Propagation studies) (Cervera & Harris, 2011). It is a widely used ray-tracing tool that models propagation through a user-defined model ionosphere. We use PHaRLAP to simulate the performance of these SuperDARN radars by employing its two-dimensional ray trace tool and applying it to different model ionospheres.

As illustrated in Figure 3, our Python program finds the operating parameters of the input SuperDARN radar using DaViTPy functions. For each time input to the Matlab wrapper, the file containing the corresponding ionospheric model output data is loaded into the program. For each beam of each radar the program uses a gridded interpolation to make a slice of the modeled ionosphere along the specified azimuth. Then the 2-D ray trace PHaRLAP function is called with the electron density grid, initial conditions, and distinct ray elevations as inputs. Each elevation angle corresponds to a different ray that the function traces until any of the following occur: the ray exits the ionospheric grid, the ray encounters an irregularity, or the ray reaches

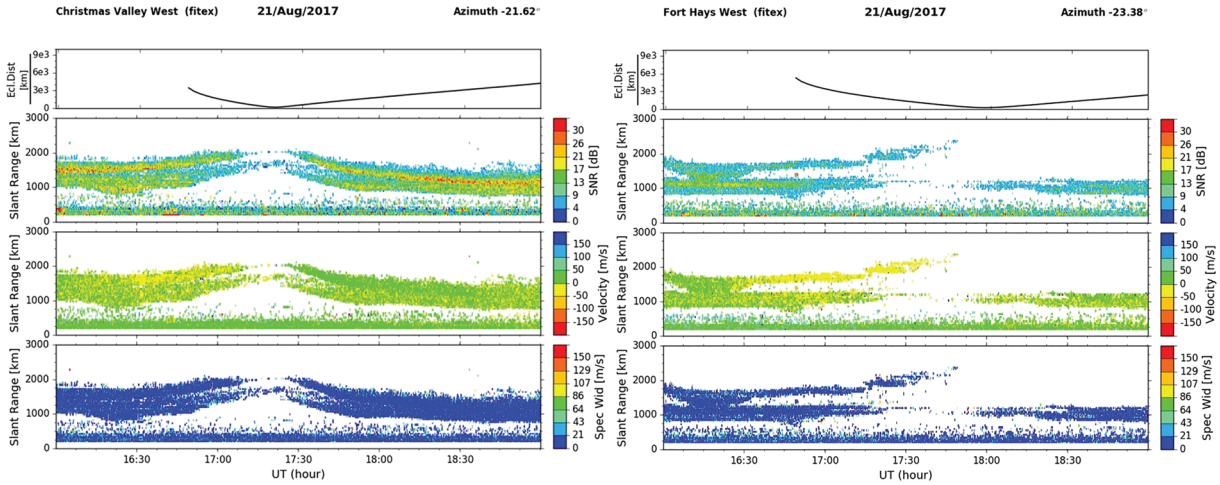

Figure 4. RTI plots (second to fourth rows) of signal-to-noise ratio (SNR), velocity, and spectral width (Spec Wid) data from camping beams of the CVW (left) and FHW (right) radars. As indicated in the first row's plot of the eclipse center's distance (Ecl.Dist) from the radar (in km), the eclipse center passes closest to CVW at about 1715 UT, and closest to FHW at about 1745 UT.

the ground within the specified number of hops. In the SuperDARN simulation the hop limit is set to 1, and multihops are assumed to be negligible; it is shown a posteriori that this is a reasonable assumption.

For each time, radar, and azimuth, the process saves a file containing the output ray trace data for all of the user-specified elevation angles. Returning to the Python program, appropriate ray trace path data are loaded from the files into a data frame, filtering out any ray path data from rays that do not return to the ground. This approach tacitly assumes that the predominant scatter observed by SuperDARN is ground scatter; it will be shown a posteriori that this also is a reasonable assumption. The path length is extracted for each of the paths for each time, along with other parameters that are analogous to measurements by the SuperDARN radars (i.e., elevation angle, etc.). These data are binned into range gates corresponding to discrete path length intervals. Values in the same range gate are averaged or counted (depending on the parameter) and are stored for future use.

2.4. Ionospheric Modeling

Ionospheric conditions are generated to represent the environment through which the simulated ray paths propagate. Background ionospheric specification is achieved using the NRL code SAMI3 (Sami is Another Model Ionosphere-3D). SAMI3 is a comprehensive three-dimensional (3-D) simulation model of Earth's ionosphere/plasmasphere system (Huba et al., 2008). Under normal simulation conditions, SAMI uses the empirical solar extreme ultraviolet (EUV) flux model for aeronomic calculations (EUVAC) to calculate photoionization and heating rates. In order to impose conditions consistent with the eclipse, we include a spatiotemporally dependent EUV scaling factor to the EUVAC spectrum. This fully 4-D scale factor, henceforth referred to as the "Drob eclipse mask," is computed using Earth/Moon/Sun ephemeris position calculation with the Naval Observatory Vector Astrometry Software (Kaplan et al., 2011) and solar flux images from the Solar Dynamics Observatory (SDO) Atmospheric Imaging Assembly (Lemen et al., 2011) measured on the day of the eclipse.

3. Data and Analysis

3.1. SuperDARN Data

One of the most common methods of presenting SuperDARN data is a Range-Time-Intensity (RTI) plot. In this format the range of each datum from the radar is plotted over time with the color indicating the observed value (i.e., SNR, velocity, etc.). RTI plots generated with DaViTPy functions also include optional top panels with plots of additional data on the operation modes and local conditions such as sky noise. For this study we plot the ground distance between the center of the umbra and the radar over time in one of these top panels. This eclipse parameter helps to give a general representation of the times of the eclipse onset, maximum, and end for comparison to measured data.

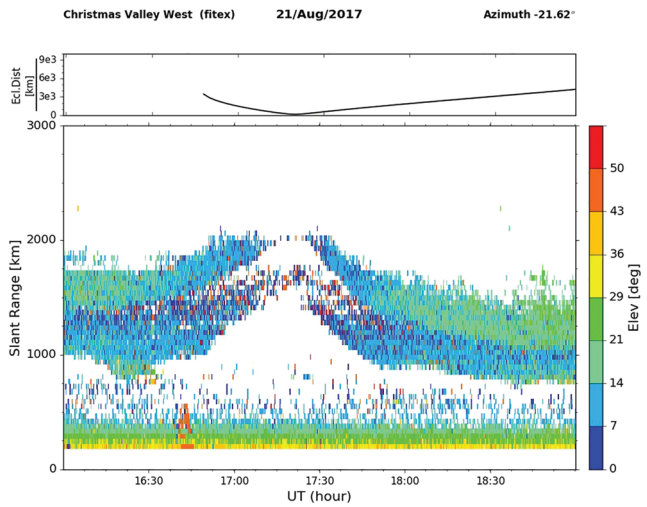

Figure 5. Christmas Valley West camping beam elevation (Elev) angle (in degrees) RTI plot (bottom panel). The top panel's plot of the eclipse center's distance (Ecl.Dist) from the radar (in km) shows that the eclipse center passes closest to CVW at about 1715 UT.

The RTI plots in Figure 4 show data from the CVW and FHW camping beams during the eclipse experiment. In both cases the observed scatter from ranges less than 630 km is fairly constant during the eclipse, as expected since scatter from these slant ranges commonly seen in SuperDARN data are typically classified as meteor scatter and/or sporadic *E* scatter (linked to neutral turbulence in the lower *E* region) (Nishitani et al., 2019). Henceforth we use the word scatter to refer to signals observed at ranges beyond the 630 km range gate. The low spectral widths and velocities shown in Figure 4 indicate that the majority of scatter measured on the eclipse day is *E* region and/or *F* region ground scatter, not ionospheric scatter. Thus, the observed changes in range are likely changes in the signal path length through the ionosphere rather than the appearance or disappearance of an ionospheric irregularity. It is noteworthy that the observed scatter ranges are clustered into two groups or scatter bands. This is commonly observed in ray trace plots and in SuperDARN and other over-the-horizon radars. It represents refraction of the signals along two or more different paths through the ionosphere, where each path corresponds to a different beam elevation and therefore different angles of incidence on the bottomside ionosphere. For example, refraction at low-elevation angles in the *E* region gives shorter path lengths than refraction at higher elevations in the *F* region, even though both signals are at the same frequency.

The observed eclipse response varies with radar site, time, and look direction. In all cases significantly less return power is received during the eclipse period, indicating that much of the transmitted energy that would normally reflect back to the receivers is lost during the eclipse. However, for reasons we cannot yet explain, plots of data from both radar sites show a much stronger eclipse signature from their westward looking camping beams than from the eastward looking camping beams. In this paper we focus on only the westward looking directions and leave the investigation into the causes of the differences in the eastward and westward beams to future studies. Both the CVW and FHW camping beams observe an increase in the path length of scattered signals near the onset of the eclipse, although the temporal responses differ between the two sites. Posttotality (1715–1800 UT) the CVW camping beam observes a steady recovery to preeclipse conditions that is nearly the mirror image of the onset period (1630–1715 UT). In contrast, the FHW camping beam shows a similar onset signature (1700–1745 UT) but does not observe a symmetric recovery to preeclipse conditions after totality (1745–1830 UT). The obvious differences between the two sites include their magnetic dip and declination angles, as well as the local time at which the eclipse maximizes, but it is not clear how any of these could produce the asymmetric scatter signature observed at the Fort Hays site.

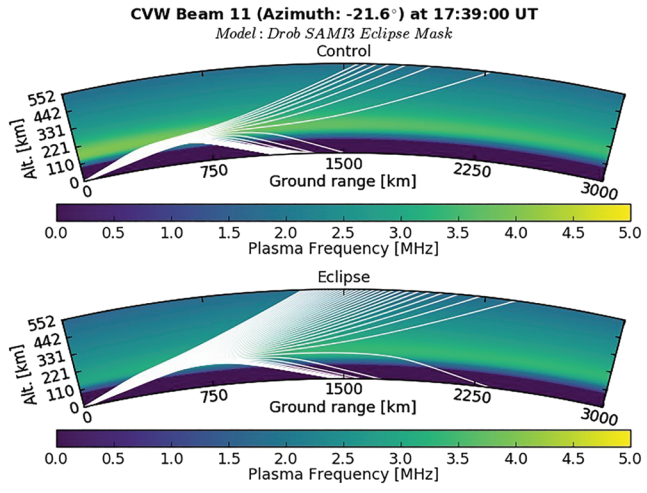

Figure 6. Comparison of ray traces through normal (top plot) and eclipsed (bottom plot) ionospheres generated by the SAMI3 model. The initial elevation angles of the rays are 10–20° in 0.25° steps. The propagation frequency in both plots is 10.534 MHz, which corresponds to the SuperDARN radar data shown in earlier figures.

The CV radars also measured the elevation angle of returned scatter during the eclipse. CVW camping beam data are plotted in Figure 5. The color scales indicate the elevation angles, so these data show that the elevation angles of returned scatter are small. Additionally, the range of scatter from higher elevations at this azimuth increases and nearly disappears around the maximum eclipse time, leaving only scatter from lower elevations. This suggests that the signals at higher elevations escape the ionosphere or travel further than the maximum range that the receiver can measure. At the same time, the slant range of scatter from these lower elevations dramatically increases.

3.2. Modeled Eclipse HF Ray Path Changes

Our propagation modeling study includes improvements to the eclipse masking function imposed on SAMI3 and ray tracing to better understand the mechanism that changes the propagation paths during the eclipse.

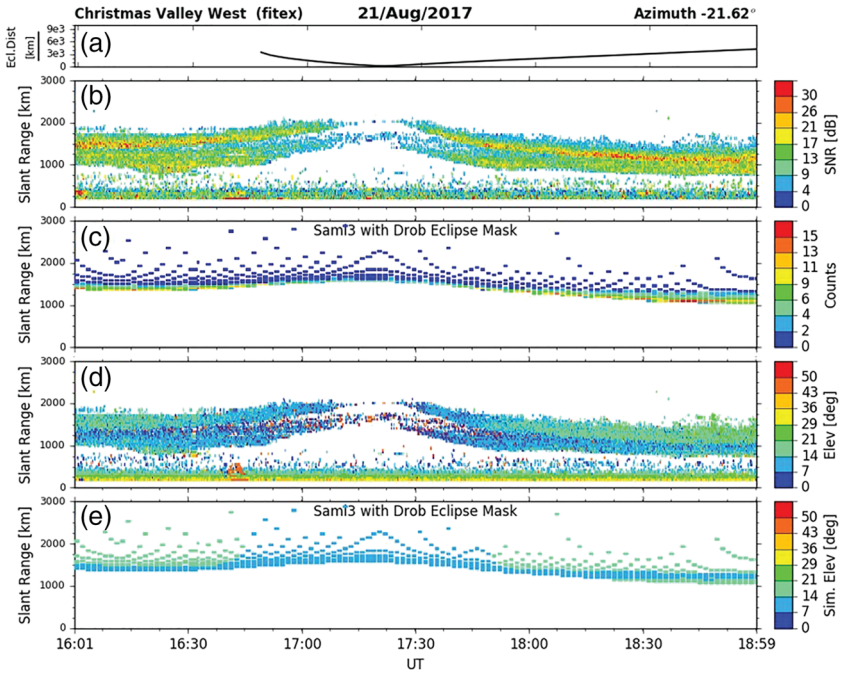

Figure 7. Comparison of simulated and measured data during the eclipse, where the Drob eclipse mask is used in the initialization of the SAMI3 model. (a) Eclipse geometry panel (distance [km] of the eclipse center from radar [Ecl.Dist]); (b) measured signal-to-noise ratio (SNR) of signals received by the SuperDARN radar; (c) the number of simulated rays in each range gate; (d) measured angle of arrival (Elev) for returned scatter; and (e) simulated initial elevation angle (Sim. Elev) of ground scattered rays, assumed to be equivalent to angle of arrival of the reflected rays.

Figure 6 shows the output for a spread of take-off angles along CVW beam 11 (azimuth −21.62°) at a frequency of 10.534 MHz (the average SuperDARN operating frequency during eclipse operations) for both the normal ionosphere (top) and the modeled ionosphere during the eclipse (bottom). The model of the eclipsed ionosphere was generated by imposing the Drob eclipse mask described in section 2.4 on the EUV radiation input to the SAMI3 model.

These plots show that significantly more power escapes through the ionosphere during the eclipse, as evidenced by the number of rays exiting the top of each panel in the figure. The low-elevation rays are preferentially refracted back to the ground and travel parallel to the Earth's surface over longer distances than the uneclipsed rays at the same elevation. In the uneclipsed case the majority of the rays return to ground roughly 1,100 km from the radar, but during the eclipse this range grows to nearly 1,500 km. This coincides with the fact that the rays that return to Earth in the eclipsed case are refracted from slightly higher altitudes than rays with the same take-off angles in the control case. As illustrated by the plasma frequency data represented by the colors in Figure 6, the altitude of the peak electron density is approximately the same in both the eclipsed and uneclipsed models, but the peak value of the plasma frequency is much lower in the eclipsed case. Therefore, these ray traces show that the increase in slant range observed by SuperDARN during the eclipse is consistent with ducting of the signal through the eclipsed region rather than a change in ionospheric layer height.

3.3. Expected HF Propagation Using PHaRLAP With Eclipsed SAMI Model

After the publication of Huba and Drob (2017), NRL and VT developed an improved EUV masking function, which we refer to as the Drob eclipse mask. The simulated SuperDARN data for the model ionosphere produced by imposing this mask on the input EUV radiation used by the SAMI3 (Hairston et al., 2018) model is given in Figures 7c and 7e. As the figure shows, imposing the Drob eclipse mask produces simulated data with elevation angles very close to the measured values, as shown in Figures 7d and 7e. This comparison of simulated and measured data also validates our use of the single-hop assumption, because the simulated one-hop path lengths are comparable to the measured slant ranges.

Table 1
For Each SuperDARN Site, the Magnetic Declination and Dip Angles and the Beam With Data That Best Align With the Local Magnetic Declination

	Magnetic field			
Site	Declination	Dip	Best aligned beam	Azimuth
Christmas Valley	14.3°	66.1°	CVE Beam 0	16.74°
Fort Hays	4.8°	66.3°	FHW Beam 19	2.54°

During the onset of the eclipse these simulated data follow the measured data fairly closely in time. However, the recovery period of these simulated data is a bit longer than that of the measured data. Additionally, the change in path length during the eclipse relative to preeclipse conditions is smaller in the simulation than in the measurements. Hence, the Drob mask produces simulated data that are close to the measured data, but some phenomena associated with ionospheric eclipse dynamics are not correctly accounted for in the SAMI model, especially in the recovery period after the peak obscuration time. In the following section we investigate one possible cause of this discrepancy.

3.4. Effect of Neutral Winds on Model Results

By default SAMI3 uses the empirical Horizontal-Wind-Model (HWM) of thermospheric neutral winds (henceforth referred to as neutral winds) to set the initial neutral wind velocities (Huba et al., 2000). Since HWM is based on statistical averages from many observations, it may not give accurate values during such a rare event as an eclipse. Furthermore, since gravity waves and other motions have been observed to be created by eclipses (Stankov et al., 2017), the local neutral wind is likely to be different from the average wind given by the model. Unfortunately no neutral wind measurements during the eclipse are available at CV or FH, so the only way to study the effects of the neutral wind velocity is through modeling. We do this by imposing neutral winds in SAMI3 using both HWM winds and hypothetical wind fields, ray tracing through the resulting ionosphere produced by SAMI3, and comparing these simulated data to each other and to measured SuperDARN data. Since SAMI3 is computationally intensive, it is more efficient to run multiple case studies with SAMI2 (Sami is Another Model Ionosphere-2D) in order to perform these comparisons. This allows us to compare particular winds to their modeled effects, which develops intuition and allows particular plasma effects to be better understood.

SAMI2 (Huba et al., 2000) calculates the plasma density along a magnetic flux tube, so for consistency the simulated SuperDARN beam should be as closely aligned with the local magnetic declination as possible for accurate results (i.e., the beam azimuth should be almost equal to the declination angle of the local magnetic field). In order to compare outputs of ray traces through profiles of SAMI2 with measured data, we ray trace along the SuperDARN azimuths given in Table 1. Custom neutral wind velocities are input to SAMI2 and run for different times for both eclipsed and uneclipsed (control) ionospheres, and the Drob model is used for the eclipsed cases. The four neutral wind cases presented are (1) default wind values from HWM, (2) no wind, (3) north/south wind values from HWM with no east/west wind, and (4) east/west wind values from HWM with no north/south wind. While some of these scenarios may not be self-consistent with the large-scale winds that actually occur in nature, our goal here is not to create a physically accurate model of winds during the eclipse. Instead we are investigating how much impact various neutral wind fields are expected to have on the ionosphere and on HF waves propagating through it.

For reference, the horizontal neutral wind velocities from HWM at each site for the eclipse day are given in Figure 8. The red and blue vectors in Figure 8 show the wind vectors given by the HWM model for both sites at points in a grid that encompasses the range, altitude, and UT time of the eclipse. The left panel shows the horizontal wind vectors (northward and eastward) as functions of range, and the right panel gives the same horizontal wind vectors at each radar site as functions of time. In both panels eastward winds correspond to vectors pointing to the right, and northward winds correspond to vectors pointing toward the top of the page. The HWM wind speed is typically greater at CV than at FH, as shown in the right panel. At 18 UT (left panel), the HWM wind speed along FHW Beam 19 and CVE Beam 0 are almost equal at long ranges. Additionally, at *F* region altitudes the HWM wind direction at both sites is toward the northwest throughout the entire time period of interest.

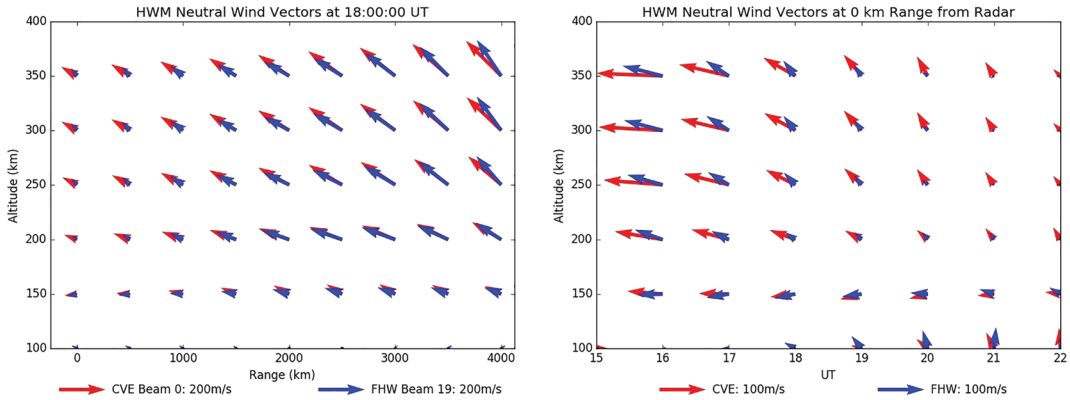

Figure 8. HWM neutral wind vectors (north is positive *y*, and east is positive *x*) over altitude versus range along the indicated beam (left plot) and altitude versus time (right plot) at Christmas Valley East (red) and Fort Hays West (blue).

In order to more easily compare the temporal evolution of the ray trace profiles, we present in Figure 9 a custom line plot visualization scheme. For each simulated time the path lengths (or slant ranges) of all rays that return to Earth within preset range bins are averaged together to obtain the mean path length of the simulated ground scatter in that bin. These averages are then plotted as dots on a separate plot that shows path length as a function of UT time for both the control day (green) and the eclipse day (red). The minimum and maximum path lengths that return to ground are plotted as vertical bars through these points. The average path lengths are plotted over time with their spread in range indicated by the vertical bars through each point and their extrema indicated by the short horizontal bars at each end. Creating such plots for both eclipsed and uneclipsed days with the four different assumed wind fields allows useful comparisons to be made.

The line plot format provides a convenient summary of both *E* layer and *F* layer propagation. The temporal evolution of the upper and lower extrema gives an indication of the variation of *F* layer and *E* layer scatter, respectively, over time. Additionally, at a given time, the relative value of the average path length as compared to the minimum and maximum values indicates which layer favors propagation at that time. A point with no vertical/horizontal bars, as is the case for the maximum eclipsed average path length in Figure 9, indicates that either only one ray reaches the ground or all rays that reach the ground have nearly identical path lengths. Similarly, one of the error bars could be partially or completely obscured by the average path length dot if the majority of rays have path lengths close to one of the extrema. Both of these conditions indicate that only one layer supports significant propagation at that time. The sensitivity of *F* layer propagation to changes in the neutral winds is easily determined by comparing the evolution of the upper bars and mean path points over time in the plots for different neutral winds.

In Figures 10–13 we present the simulated results for the four different wind cases tested, using the format defined in Figure 10. The transmitter frequency in each plot is 10.534 MHz. The line plots from ray traces through the output of SAMI2 for each of the four neutral wind cases are shown for CV in Figure 10 and for FH in Figure 11. At each site the control data vary only slightly between different wind cases, which is reasonable because the ionosphere is quasi-laminar, so no large plasma gradients are produced by the winds. During the eclipse, however, the data vary substantially with neutral wind and are also quite different at the two radar sites. This is understandable because the eclipse produces plasma density gradients, and horizontal winds acting on an ionosphere that has such gradients redistribute the plasma by moving it up and down the flux tubes, either reinforcing or opposing the diffusion driven by the density gradients.

During the eclipse period at each site and in all wind cases, the path length of the rays increases while the number of rays that return ground scatter decreases. This is indicated by the shorter vertical bars in the ray trace profiles during the eclipse periods. In each wind case at CVE, except for "HWM," there is a period around eclipse maximum where no rays return to the ground. In contrast, for every wind case at FHW one or more rays produce ground scatter at every modeled time, even during the peak of the eclipse. Another difference between the two sites is that during eclipse onset the maximum path lengths at FHW, in most wind cases, are greater than those of CVE during eclipse onset. In contrast, during the recovery phase and posteclipse, the spread of path lengths are usually greater at CVE than at FHW.

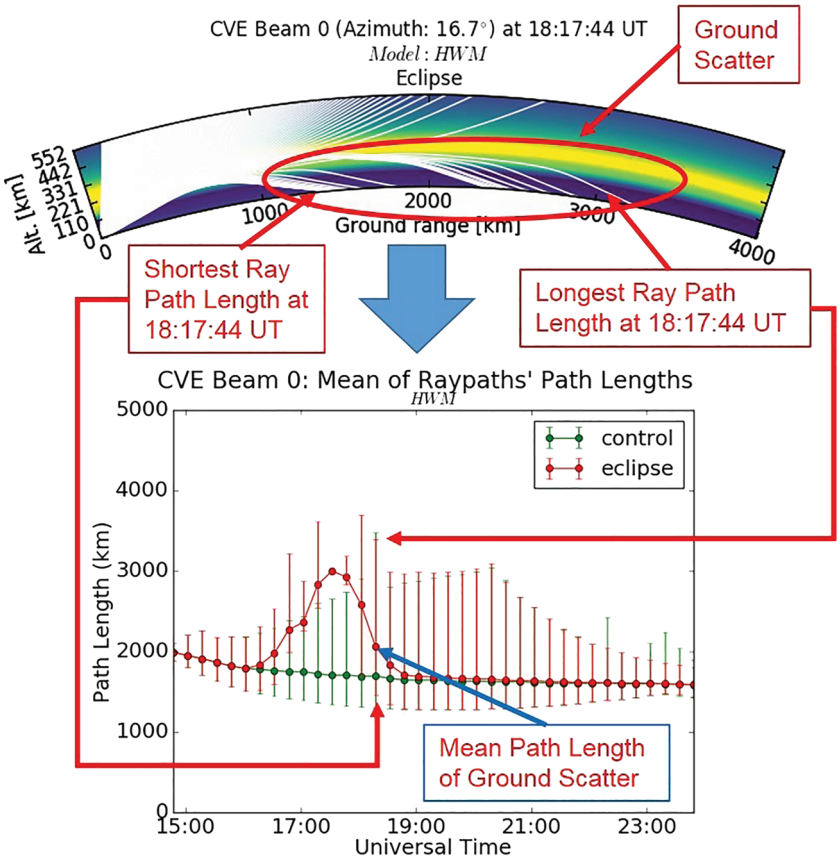

Figure 9. Process for converting eclipse case ray trace data from a profile visualization to a line plot visualization. Green/red points and error bars show the mean path lengths and their variation for control/eclipse simulations.

When comparing the eclipse plots of different wind cases, a feature of note is that at each site the Only HWM East/West Wind plot is almost identical to the No Wind plot at both sites. In contrast, the Only HWM North/South Wind plot at each site differs significantly from the No Wind plot. This suggests that the eastward wind does not have as much impact on the plasma densities as the northward wind and is consistent with the simple idea that winds having larger components in the same direction as the north-south magnetic field are able to redistribute plasma more effectively. However, the east-west wind does have some effect on the ionospheric eclipse response at CVE, because the Only HWM North/South Wind plot differs significantly from the HWM plot. FH simulations do not show a similar effect. In the former case at CVE there is a short interval in which all the rays escape near the maximum of the eclipse, whereas in the HWM plot there is always at least one ray that produces a ground scatter return. There is almost no difference between FHW's HWM and Only HWM East/West Wind eclipse plots, suggesting that the east-west wind plays almost no role in the ionospheric eclipse response at FHW.

3.5. Comparison of Modeled Data to Measured Data

A comparison between the ray trace outputs from the model wind study and the measured SuperDARN data is presented in Figures 12 and 13. The green dots and vertical lines show the SuperDARN data and are the same for all four plots at each site. The red dots and vertical lines show the simulated eclipse data. Significantly, the measured data from CV (green) show a loss of signal around the time of totality, as do the model results (red) for all but the HWM wind case. Neither the measured nor the simulated data at FH experience a total signal loss around totality. Additionally, none of these FHW simulated data appear to follow the same trends as the measured data at eclipse onset.

Although some of these SAMI2 models show features that resemble characteristics of the radar observations in time, all of the SAMI2 model results consistently overestimate the observed SuperDARN propagation path

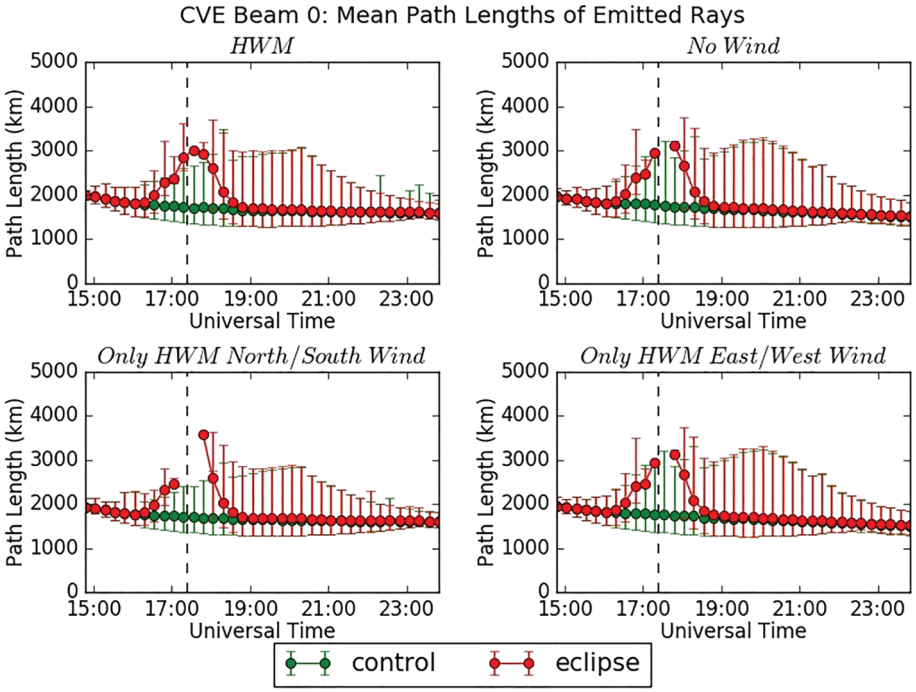

Figure 10. Line plots from ray traces through the output of SAMI2 models initialized with four different wind models at Christmas Valley. The time at which the eclipse center is closest to the radar is indicated by the vertical dashed line in each plot.

lengths. This indicates that one or more aspects of the ionospheric response during the eclipse are not correctly accounted for in the SAMI2 model. For example, eclipse-induced changes in the electron temperature (Rishbeth, 1969) and plasma diffusion are both collision-related effects, and collision frequencies of various species may be overestimated or underestimated in the eclipse model. Further modeling work will be necessary to better understand the discrepancies in the modeled propagation path lengths. However, these comparisons provide further support to our conclusion that variations in the neutral winds have a striking impact on SAMI's results and that the default HWM wind may be not sufficient for a SAMI3 eclipsed ionosphere model.

4. Discussion

4.1. HF Radar Propagation Modeling Results

The dominant effects of the 2017 eclipse on SuperDARN HF coherent scatter radar data at Christmas Valley, Oregon, and Fort Hays, Kansas, were an increase in slant range and a simultaneous decrease in the number of rays returned to the receivers, relative to preeclipse observations. The latter statement implies that the total amount of transmitted radar power escaping into space increases when the rays travel through the eclipsed ionosphere. The low velocities and small spectral widths of the SuperDARN data obtained during the eclipse indicate that the radar returns are due to ground scatter, not to irregularities produced during the eclipse. The ray trace model simulates SuperDARN ground scatter, and the dominance of ground scatter in these SuperDARN measurements strengthens the comparisons between these data and our models. Additionally, the existence of elevation angle data at the Christmas Valley radar allows for additional validation of the performance of the models. Our ray trace profiles (Figure 6) through eclipsed and uneclipsed SAMI3 models of the ionosphere indicate that rays were ducted over long horizontal paths through the depleted plasma in the eclipsed region. Thus, the observed increase in slant range in the SuperDARN observations is likely due to ducting of rays through the eclipsed region instead of a change in layer altitude. Additionally, the model results agree with three additional radar observations: (1) The unperturbed ionosphere refracts more rays back toward the Earth than does the eclipsed ionosphere; (2) both *E* and *F* region modes support longer ray paths during eclipsed conditions; and (3) the returned radar signals have smaller elevation angles (angles of arrival at the receiver) during the eclipse. This result is also consistent with amateur radio propagation

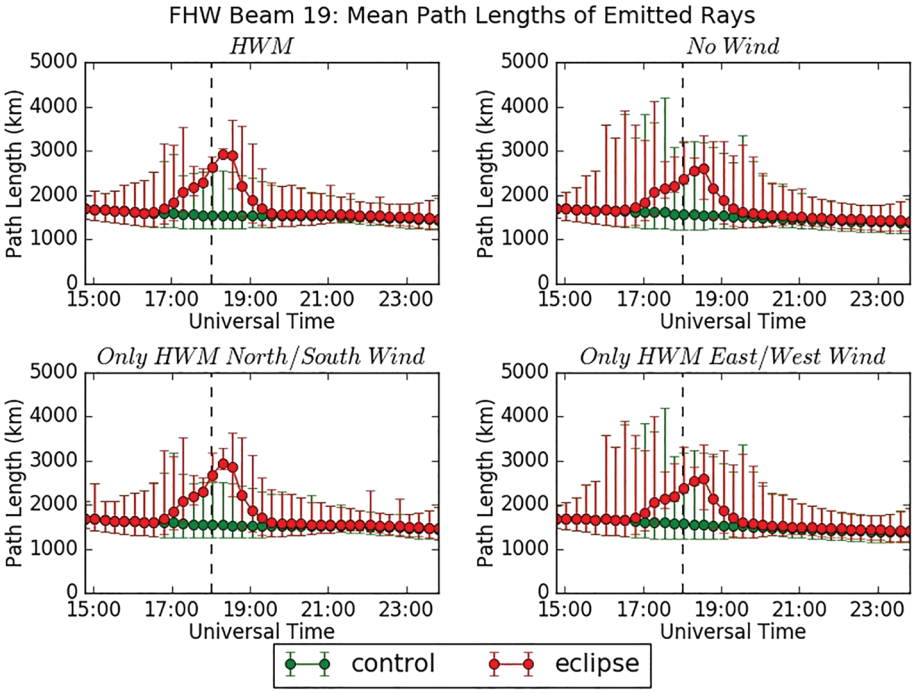

Figure 11. Line plots from ray traces through the output of SAMI2 models initialized with four different wind models at Fort Hays. The time at which the eclipse center is closest to the radar is indicated by the vertical dashed line in each plot.

studies carried out during the eclipse, in which long-distance communication links at low HF frequencies increased for propagation paths through the eclipsed regions (Frissell et al., 2018).

These effects are related to the lower plasma frequencies during the eclipse, which reduces the refractive angles by Snell's law:

$$n_0 \sin\theta_0 = n_1 \sin\theta_1 \tag{1}$$

where n_0 and n_1 are the refractive indices of two adjacent media and θ_0 and θ_1 are the incidence angles of the ray measured relative to the normal of the interface between n_0 and n_1. Since the neutral atmosphere has an index of refraction of unity that does not vary during the eclipse, we can apply Equation 1 to the eclipsed and uneclipsed cases at this interface and obtain

$$n_u \sin\theta_u = n_e \sin\theta_e \tag{2}$$

where subscripts u and e denote the value of the given variable under uneclipsed and eclipsed conditions, respectively. To first order the index of refraction is related to the plasma frequency of the ionosphere (ω_p) and the frequency of the ray (ω) by

$$n = \sqrt{1 - (\omega_p/\omega)^2} \tag{3}$$

(Hargreaves, 1992). Since we know that the eclipsed ionospheric plasma frequency is less than the uneclipsed ionospheric plasma frequency, the index of refraction will be greater during the eclipse than under normal conditions for the same radio frequency. Hence, the angle of refraction during the eclipse will decrease relative to normal conditions. A larger number of rays at a given frequency will therefore escape the eclipsed ionosphere than would escape under normal conditions because the maximum take-off angle a ray can have in order to be refracted back to the ground decreases.

Comparison of simulated propagation data with measured SuperDARN data indicate that our one-hop assumption is reasonable, because the simulated one-hop path lengths are comparable to the measured slant ranges for all eclipse masks we have tested. The eclipse mask used in the simulations shown herein is a high-resolution model of the obscuration as a function of latitude, longitude, altitude, and time. In general

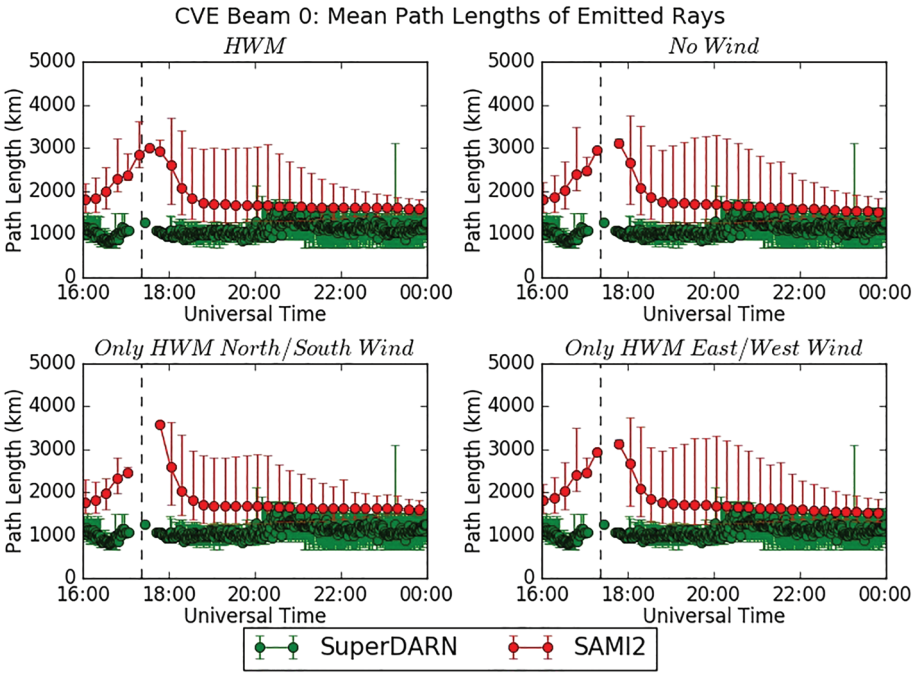

Figure 12. Line plots comparing wind study eclipse simulations to measured CVE slant range data (past Range Gate 10) with the time at which the eclipse center is closest to the radar indicated by the vertical dashed line.

it agrees well with the radar measurements during the onset phase of the eclipse, but the modeled recovery time in the period after the maximum eclipse time is longer than the time observed by the radar systems. This indicates that further improvements to the SAMI model are necessary to correctly model eclipse dynamics as the ionospheric density builds up in the recovery phase. The most obvious parameter that may be incorrectly modeled is the neutral winds, particularly any short-lived neutral wind perturbations induced by pressure

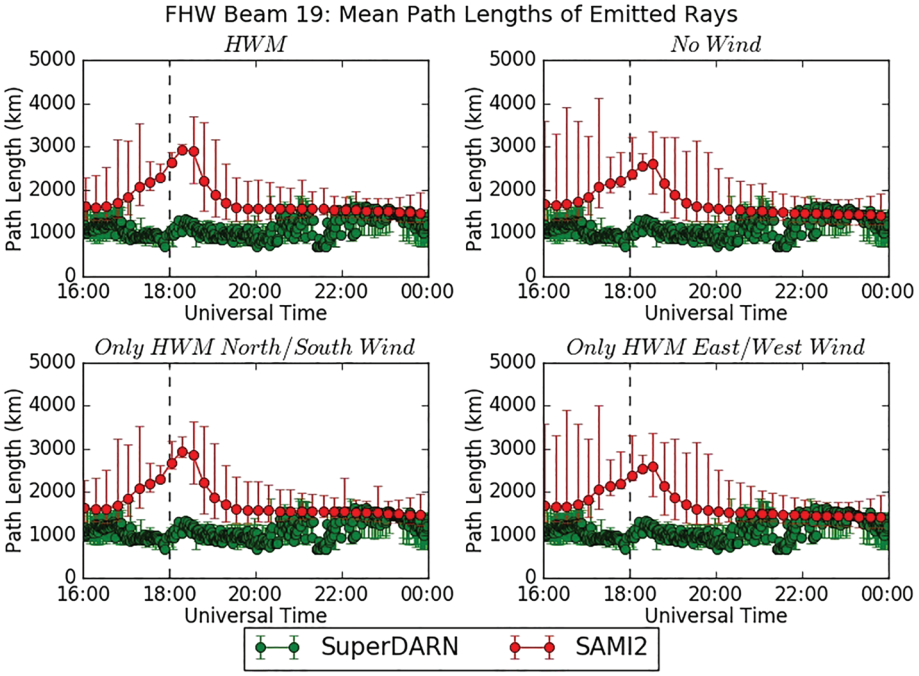

Figure 13. Line plots comparing wind study eclipse simulations to measured FHW slant range data (past Range Gate 10) with the time at which the eclipse center is closest to the radar indicated by the vertical dashed line.

gradients caused by the eclipse. We study the importance of this effect by using the SAMI2 model and the ray-tracing code to investigate the impact of horizontal neutral winds on propagation conditions during the eclipse.

4.2. Effects of Neutral Winds

At both radar sites the hypothetical modeled variations in the meridional neutral wind velocity produce larger eclipse propagation changes than do cases with zero net wind or cases with variations in only the zonal neutral wind. The meridional winds are therefore expected to have a greater impact on the eclipsed ionosphere than zonal winds. North-south winds also move plasma vertically along the flux tubes, and depending on the wind direction this will either increase or offset the ambipolar diffusion of plasma from uneclipsed regions of the flux tube into regions affected by the eclipse.

In order to more fully explain these phenomena, the neutral wind-induced plasma drift equations must be examined. The steady-state drift velocity (V) of some plasma species j due to a neutral wind with velocity U can be determined by solving the steady-state equation of motion given in Rishbeth and Garriott (1969). The resulting expression is

$$\vec{V}_j = \frac{1}{\omega_j^2 + \nu_j^2}\left(\nu_j^2\vec{U} + \omega_j^2\frac{(\vec{U}\bullet\vec{B})\vec{B}}{|\vec{B}|^2} + \nu_j\omega_j\frac{\vec{U}\times\vec{B}}{|\vec{B}|}\right) \tag{4}$$

where ν_j is the particle-neutral collision frequency of species j, ω_j is the gyrofrequency of species j, and $\vec{B}$ is the local magnetic field. The three separate terms in this equation may be called the direct, parallel, and perpendicular components, respectively. At F region altitudes the perpendicular and direct components are negligible compared to the parallel term, due to the relative magnitudes of the collision frequency and the gyrofrequency for both electrons and ions. Therefore, the component of the wind that is most closely aligned to the magnetic field will have the greatest impact on the wind-induced drift velocity at high altitudes. Since the geomagnetic field generally has its largest component in the north-south-zenith-nadir plane, one would expect the east-west (zonal) component of the wind to have less effect on plasma motions than the north-south (meridional) component. Note that vertically directed winds would also be very important, but it is well known that the horizontal components of the thermospheric wind are generally much larger than the vertical winds, so this component can generally be neglected.

The declination angle of the horizontal magnetic field at both sites (given in Table 1) is very small, so a meridional wind is much better aligned with the magnetic field at both sites than a zonal wind. The direction of the horizontal component of the magnetic fields at the two SuperDARN sites differ from one another by about 10°, while the dip angles of the field at the two sites are quite similar. Thus, the ionosphere will respond differently at each site in response to the same neutral wind. Since the horizontal magnetic field is more northward directed at Fort Hays, the plasma drift velocity there will not change quite as much as that at Christmas Valley for the same change in wind magnitude. This explains why the simulated cases having only north-south winds agree better with the simulated HWM cases for Fort Hays than for Christmas Valley.

The studies shown here demonstrate that the combination of SAMI modeling and ray tracing may be a useful approach for examining the wealth of factors that affect the ionospheric plasma during eclipses. Our simulated wind study confirms that as the magnetic declination angle decreases, changes in the north-south wind at F region altitudes should have a more significant impact on the wind-induced drift velocity than changes in the east-west wind. Furthermore, the coupling of SAMI model outputs with the ray-tracing algorithm allows us to confirm the ducting of HF radiation over long distances through the eclipsed ionosphere as confirmed by direct comparison against SuperDARN HF radar observations at two different geographical sites.

5. Summary and Conclusions

During the 2017 eclipse the SuperDARN radars at Christmas Valley (CV) and Fort Hays (FH) observed an increase in slant range and a decrease in the number of rays that were refracted back toward the Earth relative to preeclipse observations. The low velocities and small spectral widths of these SuperDARN data confirm that the majority of observed scatter before, during, and after the eclipse was ground scatter. Additionally, the CV radars observed decreases in angles of arrival (elevation angles) of returned scatter during the eclipse, which is generally consistent with longer propagation paths through the ionospheric F region. However, the signatures of eclipse-induced ionospheric perturbations in the data from the FH and CV radars

(i.e., slant range increase, decrease in the amount of returned scatter, and decrease in elevation angles of returned scatter) become less pronounced or vanish entirely as a given radar looks away from the west and toward the east. The westward looking CV eclipse data are symmetric in time about the maximum of the eclipse at the site, but the westward looking FH eclipse data are asymmetric in time, with the recovery period lasting much longer than the onset period.

The details of the nature of this phenomenon will be the subject of future investigations; however, we hypothesize that this difference between the eclipse responses observed at CV and FH may stem from their somewhat different declinations and/or from the fact that the eclipse occurred in the early morning at CV and near local noon at FH. Both of these factors affect how much plasma is available within a flux tube to replenish the plasma depleted by the eclipse. Because the magnetic field at CV is more east-west directed than at FH, the flux tube at CV is less aligned with the line of sight to the Sun in the morning than is the FH flux tube at local noon. Furthermore, the *F* region plasma density at high altitudes in the flux tube passing over CV would be relatively low when the eclipse occurred, while it would have been much higher at noon, especially on a flux tube that was fully illuminated some distance above and southward of the eclipse zone. In other words, not all of the plasma along the flux tube passing through *F* region altitudes at CV would have been depleted by the eclipse because the Sun would not have been well aligned with the flux tube. Thus, plasma from higher altitudes could have diffused more rapidly along the flux tube at CV in response to the plasma density gradient created by the eclipse. In contrast, since the eclipse occurred at noon at FH, the overall plasma density within the flux tube would have been higher, and the flux tube would have been reasonably well aligned with the Sun. Field-aligned diffusion, cross-field diffusion, chemical production and loss, and even convection from electric field perturbations associated with the eclipse must be considered to fully understand the ionospheric response to the eclipse. Based on the studies shown herein, we suggest that the SAMI model is an appropriate tool for this task, and coupling it with a ray-tracing model is an excellent way to make comparisons to the SuperDARN radar data.

Our analysis involves comparing simulated radar data with measured radar data from two midlatitude SuperDARN sites. The model ionospheric density profiles are generated by imposing an eclipse masking function on the EUV input to the SAMI numerical model. A ray trace simulation of SuperDARN is then run using these modeled ionospheric profiles to generate simulated SuperDARN ground scatter data. Comparisons between measured and simulated time scales and elevations at CV allows us to test the accuracy of the SAMI models and the EUV mask. Our work demonstrates that this is a useful technique for studying how various forcing terms can affect the HF propagation during eclipses.

Using these methods we show results from several initial studies: (1) an investigation of the nature of the increase in slant range during the eclipse, (2) a validation of the SAMI model during eclipse conditions, and (3) a model-based study of the impact of neutral wind direction on eclipse dynamics. Ray trace profiles through the eclipsed SAMI3 output indicate that rays were ducted through the depleted plasma in the eclipsed region, and the agreement between the theoretical model results and the SuperDARN data is generally good, especially as related to the onset and recovery at the Christmas Valley site. However, the eclipse mask imposed in SAMI3 produces simulated data in which the ionospheric recovery times are somewhat longer and the elevation angles slightly higher than that observed by SuperDARN during the actual eclipse. This indicates that further improvements to the simulation approach or better knowledge of neutral wind fields during the eclipse is necessary to correctly model eclipse dynamics.

We use the SAMI model and the PHaRLAP ray-tracing code together to more deeply investigate the impact of variously directed neutral winds on HF propagation during the eclipse. One result of this study is that the meridional neutral winds are expected to have a greater impact on the ionospheric eclipse response than the zonal neutral winds especially at FH. As the dominant neutral wind-induced plasma drift at *F* region altitudes is parallel to the magnetic field, we believe that the sensitivity of the ionospheric eclipse response to changes in the meridional wind stems from the primarily northward geomagnetic field orientation at both CV and FH. Since neutral winds are very difficult to measure, the models of their behavior are not as mature as the IRI and MSIS models, especially during unusual phenomena like eclipses. Thus, our study highlights an additional imperative for improving thermospheric wind models and measurements.

This study has demonstrated the utility of using ray trace tools with the SAMI2 and SAMI3 models to generate comparative data for interpreting HF radar data during eclipses. Using these tools, we have shown that the increased slant range observed by the SuperDARN radars during the eclipse is likely due to ducting of

radio waves through the depleted plasma of the eclipsed region. The four-dimensional accurate scaling of the EUV flux in SAMI3 produced by the Drob mask produces output ray trace data that agree well with the observed data regarding elevation and onset time dependencies of eclipse-induced ionospheric effects. The demonstrated importance of wind direction to understanding the ionospheric eclipse response should be considered carefully in designing future experiments to study eclipse effects on the ionosphere. This is particularly relevant to the 2024 eclipse that will pass near the Millstone Hill observatory, where field-aligned plasma drifts may be measurable throughout the eclipse in addition to plasma density and temperature changes. Such measurements may provide the additional constraints needed to improve the agreement between the SAMI model outputs and direct empirical observations.

Data Availability Statement

The HF propagation toolbox, PHaRLAP, is available by request from its author (Dr. Manuel Cervera, Defence Science and Technology Organisation, Australia, manuel.cervera@dsto.defence.gov.au). The SuperDARN data sets are available in the Virginia Tech website (at https://vt.superdarn.org). Eclipse path data are available online (at https://xjubier.free.fr/en/site_pages/SolarEclipsesGoogleEarth.html).

Acknowledgments
Funding for this research was provided by National Aeronautics and Space Administration (NASA) grant NASA #NNX17AH70G, National Science Foundation (NSF) grant NSF #AGS-1552188, a Virginia Space Grant Consortium (VSGC) 2015–2016 Undergraduate Research Fellowship, and 2017–2018 and 2018–2019 VSGC Graduate Research Fellowships. The ray tracing results presented in this paper were obtained using the HF propagation toolbox, PHaRLAP, created by Dr. Manuel Cervera, Defence Science and Technology Organisation, Australia (manuel.cervera@dsto.defence.gov.au). Funding for operations of U.S. SuperDARN radars is provided by NSF grants AGS-1341925 and AGS-1934997 (for Dartmouth College) and AGS-1341918 and AGS-1935110 (for Virginia Tech). Data analysis and visualizations in this paper were generated by employing several free open-source software packages including matplotlib (Hunter, 2007), iPython (Pérez & Granger, 2007), SciPy (Virtanen et al., 2020), NumPy (van der Walt et al., 2011), and DaViTPy (Ribeiro et al., 2020), among others. Note that DaViTPy was depreciated upon the release of pyDARN (Schmidt et al., 2020) in May 2020, after the work presented in this paper was completed. Also, we acknowledge the contributions of New Jersey Institute of Technology Eclipse Team (especially Joshua Vega, Joshua Katz, and Nathaniel Frissell) to our initial development of supporting Matlab functions for the use of SAMI3 output files with PHaRLAP.

References

Afraimovich, E. L., Kosogorov, E. A., & Lesyuta, O. S. (2002). Effects of the August 11, 1999 total solar eclipse as deduced from total electron content measurements at the GPS network. *Journal of Atmospheric and Solar Terrestrial Physics*, *64*(18), 1933–1941. https://doi.org/10.1016/S1364-6826(02)00221-3

Bowhill, S. A. (1970). Ionospheric effects in solar eclipses. In M. Anastassiades (Ed.), *Solar Eclipses and the Ionosphere. A NATO Advanced Studies Institute held in Lagonissi, Greece, May 26-June 4, 1969* (pp. 3–17). New York, NY: Plenum Press. https://doi.org/10.1007/978-1-4684-1839-2

Bullett, T., & Mabie, J. (2018). Vertical and oblique ionosphere sounding during the 21 August 2017 solar eclipse. *Geophysical Research Letters*, *45*, 3690–3697. https://doi.org/10.1002/2018GL077413

Cervera, M. A., & Harris, T. J. (2011). Modelling the effects of ionospheric disturbances on quasi-vertically incident ionograms using 3D magneto-ionic raytracing. In *2011 xxxth ursi general assembly and scientific symposium* (pp. 1–4). https://doi.org/10.1109/URSIGASS.2011.6123721

Chen, G., Qi, H., Ning, B., Zhao, Z., Yao, M., Deng, Z., et al. (2013). Nighttime ionospheric enhancements induced by the occurrence of an evening solar eclipse. *Journal of Geophysical Research: Space Physics*, *118*, 6588–6596. https://doi.org/10.1002/jgra.50551

Chuo, Y. J. (2013). Ionospheric effects on the *F* region during the sunrise for the annular solar eclipse over Taiwan on 21 May 2012. *Annales Geophysicae*, *31*(11), 1891–1898. https://doi.org/10.5194/angeo-31-1891-2013

Evans, J. V. (1965a). An *F* region eclipse. *Journal of Geophysical Research*, *70*(1), 131–142. https://doi.org/10.1029/JZ070i001p00131

Evans, J. V. (1965b). On the behavior of fof2 during solar eclipses. *Journal of Geophysical Research*, *70*(3), 733–738. https://doi.org/10.1029/JZ070i003p00733

Frissell, N. A., Katz, J. D., Gunning, S. W., Vega, J. S., Gerrard, A. J., Earle, G. D., et al. (2018). Modeling amateur radio soundings of the ionospheric response to the 2017 Great American Eclipse. *Geophysical Research Letters*, *45*, 4665–4674. https://doi.org/10.1029/2018GL077324

Hairston, M. R., Mrak, S., Coley, W. R., Burrell, A., Holt, B., Perdue, M., et al. (2018). Topside ionospheric electron temperature observations of the 21 August 2017 eclipse by DMSP spacecraft. *Geophysical Research Letters*, *45*, 7242–7247. https://doi.org/10.1029/2018GL077381

Hargreaves, J. K. (1992). *The solar terrestrial environment*. New York, NY: the Press Syndicate of the Cambridge University Press.

Huba, J. D., & Drob, D. (2017). Sami3 prediction of the impact of the 21 August 2017 total solar eclipse on the ionosphere/plasmasphere system. *Geophysical Research Letters*, *44*, 5928–5935. https://doi.org/10.1002/2017GL073549

Huba, J. D., Joyce, G., & Fedder, J. A. (2000). Sami2 is another model of the ionosphere (SAMI2): A new low-latitude ionosphere model. *Journal of Geophysical Research*, *105*(A10), 23,035–23,053. https://doi.org/10.1029/2000JA000035

Huba, J. D., Joyce, G., & Krall, J. (2008). Three-dimensional equatorial spread *F* modeling. *Geophysical Research Letters*, *35*, L10102. https://doi.org/10.1029/2008GL033509

Hulburt, E. O. (1939). The *E* region of the ionosphere during the total solar eclipse of October 1, 1940. *Physical Review*, *55*(7), 646–647. https://doi.org/10.1103/PhysRev.55.646

Hunter, J. D. (2007). Matplotlib: A 2D graphics environment. *Computing in Science & Engineering*, *9*(3), 90–95. https://doi.org/10.1109/MCSE.2007.55

Kaplan, G., Bartlett, J., Monet, A., Bangert, J., & Puatua, W. (2011). User's guide to NOVAS Version F3.1, naval observatory vector astrometry software. US Naval Observatory, Washington, DC. http://www.usno.navy.mil/USNO/astronomical-applications/softwareproducts/novas/novas-fortran/NOVAS_F3.1_Guide.pdf

Lemen, J. R., Akin, D. J., Boerner, P. F., Chou, C., Drake, J. F., Duncan, D. W., et al. (2011). The Atmospheric Imaging Assembly (AIA) on the Solar Dynamics Observatory (SDO). *The Solar Dynamics Observatory* (pp. 17–40). New York, NY: Springer.

Nishitani, N., Ruohoniemi, J. M., Lester, M., Baker, J. B. H., Koustov, A. V., Shepherd, S. G., et al. (2019). Review of the accomplishments of mid-latitude Super Dual Auroral Radar Network (SuperDARN) HF radars. *Progress in Earth and Planetary Science*, *6*(1), 27. https://doi.org/10.1186/s40645-019-0270-5

Pérez, F., & Granger, B. E. (2007). IPython: A system for interactive scientific computing. *Computing in Science and Engineering*, *9*(3), 21–29. https://doi.org/10.1109/MCSE.2007.53

Pitout, F., Blelly, P. L., & Alcayd, D. (2013). High-latitude ionospheric response to the solar eclipse of 1 August 2008: EISCAt observations and TRANSCAR simulation. *Journal of Atmospheric and Solar-Terrestrial Physics*, *105-106*, 336–349. https://doi.org/10.1016/j.jastp.2013.02.004

Ribeiro, A. J., Sterne, K., de Larquier, S., Reimer, A., Wessel, M., Maimaiti, M. R. M., et al. (2020). vtsuperdarn/davitpy: Final release of davitpy. Zenodo. https://doi.org/10.5281/zenodo.3824466

Rishbeth, H. (1969). Theoretical aspects of solar eclipses. Plenum Press.
Rishbeth, H., & Garriott, O. K. (1969). *Introduction to ionospheric physics, International Geophysical Series*. New York; San Francisco, London: Academic Press Inc.
Schmidt, M. T., Detwiller, M. H., Billet, D. D., Bland, E. C., Burrell, A. G., Kotyk, K., et al. (2020). SuperDARN/pydarn: pyDARN v1.0.0 release. Zenodo. https://doi.org/10.5281/zenodo.3727270
Sivakumar, V. (2018). Summary of eclipse effects on the ionosphere: Virginia Polytechnic Institute and State University.
Stankov, S. M., Bergeot, N., Berghmans, D., Bolse, D., Bruyninx, C., Chevalier, J. M., et al. (2017). Multi instrument observations of the solar eclipse on 20 March 2015 and its effects on the ionosphere over Belgium and Europe. *Journal of Space Weather and Space Climate*, *7*, A19. https://doi.org/10.1051/swsc/2017017
van der Walt, S., Colbert, S. C., & Varoquaux, G. (2011). The NumPy array: A structure for efficient numerical computation. *Computing in Science Engineering*, *13*(2), 22–30.
Virtanen, P., Gommers, R., Oliphant, T. E., Haberland, M., Reddy, T., Cournapeau, D., et al. (2020). SciPy 1.0: Fundamental algorithms for scientific computing in Python. *Nature Methods*, *17*, 261–272. https://doi.org/10.1038/s41592-019-0686-2